Multistate Coupled Diabatic Neural Network potential for the quantum non-adiabatic Photofragmentation of CH_2^+

Pablo del Mazo–Sevillano,[a] Susana Gómez–Carrasco,[a] Alfredo Aguado,[b] and Octavio Roncero[c]

Contents

1 Potential energy matrix (PEM)

1.1 Zeroth–order PEM ($\boldsymbol{U}^0$)

The diagonal elements of $\boldsymbol{U}^0$ are expressed:

$$U^0_{ii} = V_{1B} + V_{2B} + V_{lr} \tag{1}$$

where V_{1B} are the atomic energies of the total dissociation asymptote, V_{2B} is the sum of the three possible diatomics in the diabatic state, and V_{lr} is the long range interaction of the rearrangement channel.

Each V_{2B} is the sum of three diatomic contributions:

$$V_{2B} = E_{CH^+/CH}(R_{CH^1}) + E_{CH^+/CH}(R_{CH^2}) + E_{H_2/H_2^+}(R_{HH}) \tag{2}$$

$$E_{AB}(R_{AB}) = \frac{c_0 e^{-\alpha_{AB} R_{AB}}}{R_{AB}} + R_{AB} \sum_{i=1}^{N} c_i e^{-i\beta_{AB} R_{AB}} \tag{3}$$

where c_i, α_{AB} and β_{AB} are fitted with a slight modification of the regular Aguado-Paniagua functions,[1] to reproduce the diabatic diatomic energy curves.

The long-range energy terms V_{lr}, depends of the channel. We have considered the charge-induced dipole energy for $CH^+ + H$ asymptote and the charge-quadrupole dispersion energy and charge-induced dipole dispersion energy for the $C^+ + H_2$ asymptote.[2]

[a] *Departamento de Química Física, Facultad de Ciencias Químicas, Universidad de Salamanca, 37008 Salamanca, Spain. E-mail: pablomazo@usal.es*
[b] *Departamento de Química Física Aplicada (UAM), Unidad Asociada a IFF-CSIC, Facultad de Ciencias Módulo 14, Universidad Autónoma de Madrid, 28049, Madrid, Spain.*
[c] *Instituto de Física Fundamental (IFF-CSIC), C.S.I.C., Serrano 123, 28006, Madrid, Spain. E-mail: octavio.roncero@csic.es*

1.2 Neural network correction ($\boldsymbol{U}^{NN}$)

$\boldsymbol{U}^{NN}$ is computed from a PIP–NN network which receives 22 symmetry functions of the interatomic distances and outputs 51 elements which are distributed to diagonal and non–diagonal elements of the PEM. The PIP–NN has two hidden layers with 100 neurons each connected through hyperbolic tangent activation functions. For the output layer a linear activations is employed. The AdamW optimizer [3] is employed with an initial learning rate of 0.1, which is reduced stepwise until $4 \cdot 10^{-3}$ by the end of the training process after 100000 steps. The PIP-NN is trained with and in–house Python code making use of Pytorch library. [4]

The outputs of the PIP–NN are multiplied by a damping function of the CH distances to zero them as the system tends to a 2–body or total dissociation region:

$$s(\mathrm{CH}_x) = \exp\left(-\alpha_s r_{\mathrm{CH}_x}\right) \tag{4}$$

with $\alpha_s = 0.5\, a_0^{-1}$.

The full $\boldsymbol{U}^{NN}$ matrix is:

$$\boldsymbol{U}^{NN,A'} = \begin{pmatrix} NN(1) & NN(2) & NN(3)s & NN(4)s & NN(5)s & NN(6)s & NN(7)s & NN(8)s \\ & NN(9) & NN(10)s & NN(11)s & NN(12)s & NN(13)s & NN(14)s & NN(15)s \\ & & NN(16) & NN(17) & NN(18) & NN(19) & NN(20)s & NN(21)s \\ & & & NN(22) & NN(23) & NN(24) & NN(25)s & NN(26)s \\ & & & & NN(27) & NN(28) & NN(29)s & NN(30)s \\ & & & & & NN(31) & NN(32)s & NN(33)s \\ & & & & & & NN(34) & NN(35) \\ & & & & & & & NN(36) \end{pmatrix} \tag{5}$$

$$\boldsymbol{U}^{NN,A''} = \begin{pmatrix} NN(37) & NN(38) & NN(39)s & NN(40)s & NN(41)s & NN(42)s & NN(43)s & NN(44)s \\ & NN(45) & NN(46)s & NN(47)s & NN(48)s & NN(49)s & NN(50)s & NN(51)s \\ & & NN(16) & NN(17) & NN(18) & NN(19) & NN(20)s & NN(21)s \\ & & & NN(22) & NN(23) & NN(24) & NN(25)s & NN(26)s \\ & & & & NN(27) & NN(28) & NN(29)s & NN(30)s \\ & & & & & NN(31) & NN(32)s & NN(33)s \\ & & & & & & NN(34) & NN(35) \\ & & & & & & & NN(36) \end{pmatrix} \tag{6}$$

where $s = \sin(\theta)$, being θ the H-C-H angle. The elements NN are already multiplied by the damping function.

2 Training strategy

2.1 Configuration sampling

The points to train the diabatic model are taken from a grid of points in the [CH + H]+ and C + H_2+ asymptotes. Considering in both cases Jacobi coordinates, where r is the diatomic distance, R the distance between the atom and the diatom's center of mass and θ the angle between the previous vectors, the grids are:

- $\mathbf{[CH + H]^+}$: R changes between (0.6–2.4)Å at intervals of 0.1 Å. θ is taken between (0–180)° at intervals of 10°. r is taken between (0.1–10.0) Å. For r greater than 6 Å the intervals are of 1.0 Å and 0.1 Å for lower values.
- $\mathbf{[C + H_2]^+}$: R changes between (0.5–2.4)Å at intervals of 0.1 Å. θ is taken between (0–90)° at intervals of 10°. r is taken between (0.1–10.0) Å. For r greater than 6 Å the intervals are of 1.0 Å and 0.1 Å for lower values.

With these two grids, the total number of points included in the training process are 22717.

For the training process the data is randomly divided into the training and validation sets with 80% and 20% of the data, respectively.

2.2 Hyperparameter optimization

A grid search of the optimal hyperparameter configuration has been done for the number of hidden layers, size of the hidden layers and the regularization factor, λ_2 in Eq. (3). This optimization was performed for a previous model which considered 4 adiabatic states in each A' and A'' representations. The optimal configuration was directly adopted for the current model. Other relevant hyperparameters are not optimized, as the learning rate which takes an initial value of 10^{-2} and it is reduced by a factor of 0.5 when the validation error does not

improve for 50 validation steps. A minimum learning rate is set to 10^{-3}. An AdamW optimizer is employed with the default parameters in the PyTorch implementation. The results are schematically represented in Fig. 1. In these tests all the hidden layers have the same number of neurons.

In all cases we find the expected trend, where increasing the size of the neural network results in a lower RMSE. However, the reduction of the RMSE when increasing a hidden layer with $\lambda_2 = 10^{-3}$ can be considered marginal compared to the increase in the computational cost of inference in the larger neural network. A similar argument is applied when comparing the effect of augmenting the number of neurons in the hidden layer from 100 to 200.

Our final decision is to train the models with $\lambda_2 = 10^{-3}$ with two hidden layers each of them with 100 neurons. While increasing the number of hidden neurons would have resulted in marginally better RMSEs, this cannot justify the increased computation time due to the larger neural net.

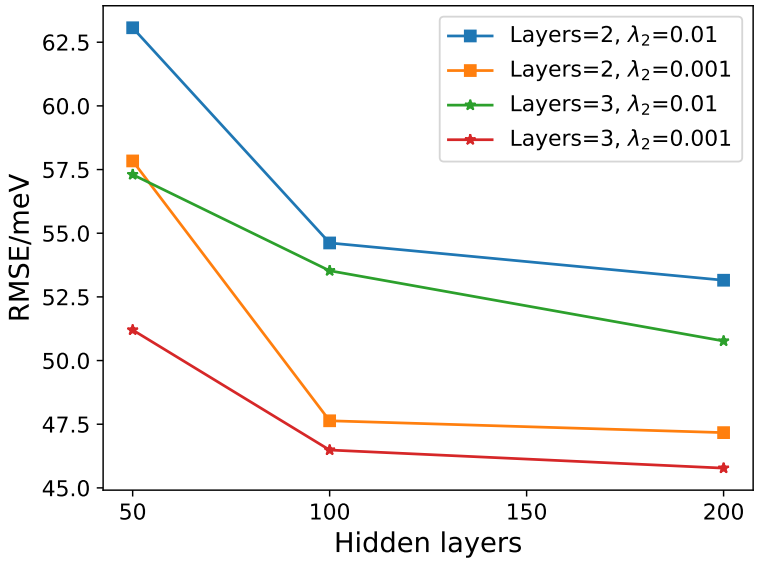

Figure 1: Representation of the final RMSE for each hyperparameter configuration, averaged over 10 runs. The x–axis represents the number of neurons in each hidden layer. Each line is a different hyperparameter configuration, which can be read in the legend.

2.3 Learning curves

The training process is run for 100k epochs where we find no significant change in the loss value, both for training and validation sets. The final parameters are taken from the step with lowest validation error. In Fig. 2 the training and validation errors are presented.

2.4 Independence of diabatic order

In our experiments we have found that the order of the diabatic states is independent from the initial random parameters of the $\boldsymbol{U}^{NN}$ term. Given the physically based zeroth order diabatic matrix, $\boldsymbol{U}^0$, all our training runs end up with optimal diabatic models which are equivalent. We can say that including a diabatization scheme for the asymptotes and specifying how are they connected imposes a strong restriction to the diabatic model in the three–body region.

In Fig. 3 we present the order of the diabatic states for some trained models.

3 Cuts of the PES

The adiabatic energies computed with the new PEM are compared with *ab initio* calculations in Figs. 4, 5, 6, and 7, which virtually cover the full range of geometries for the CH_2^+ system.

4 PES for bound states

The 8×8 diabatic PEMs are built to represent many electronic states over a large energy interval and have a relatively large error to reproduce the initial bound states with nearly spectroscopic accuracy. To improve the

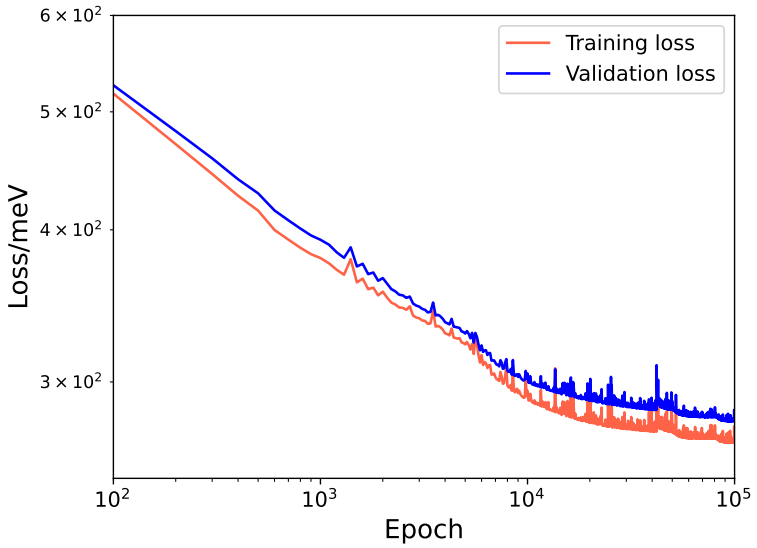

Figure 2: Representation of the training and validation loss curves along the training process for the optimal hyperparameter configuration.

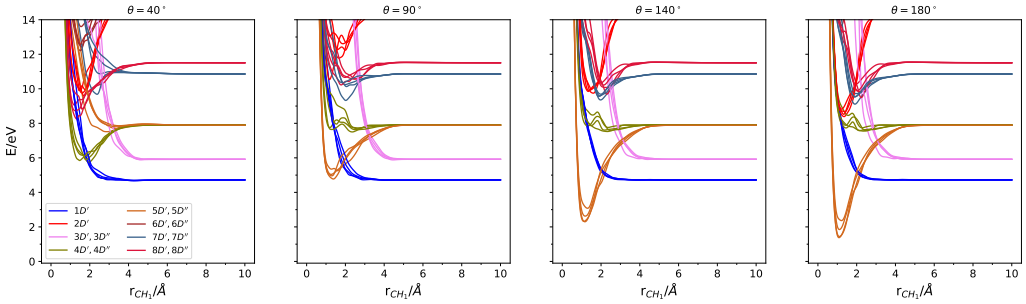

Figure 3: Representation of the order of the diabatic states for different trained models along several $[CH + H]^+$ approaches with one CH distance fixed at 1.1 Å and r_{CH_1} the distance of an incoming H. Four different H–C–H angles are represented.

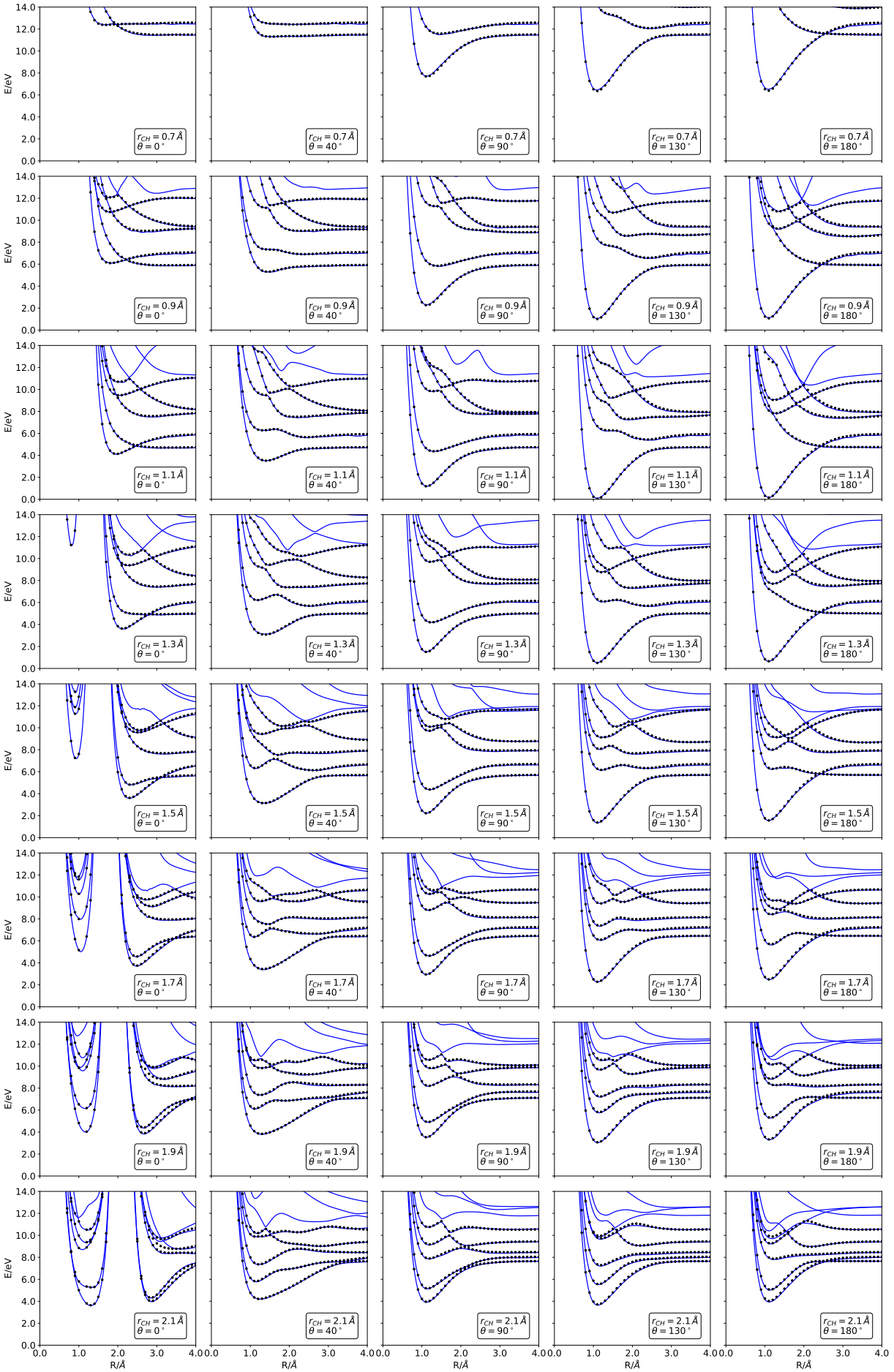

Figure 4: Adiabatic energies of the A' states computed from the PEM (solid lines) compared with *ab initio* calculation of the five lowest adiabatic states. For each CH distance (r_{CH}) and H–C–H angle (θ) the second CH distance (R) is scanned.

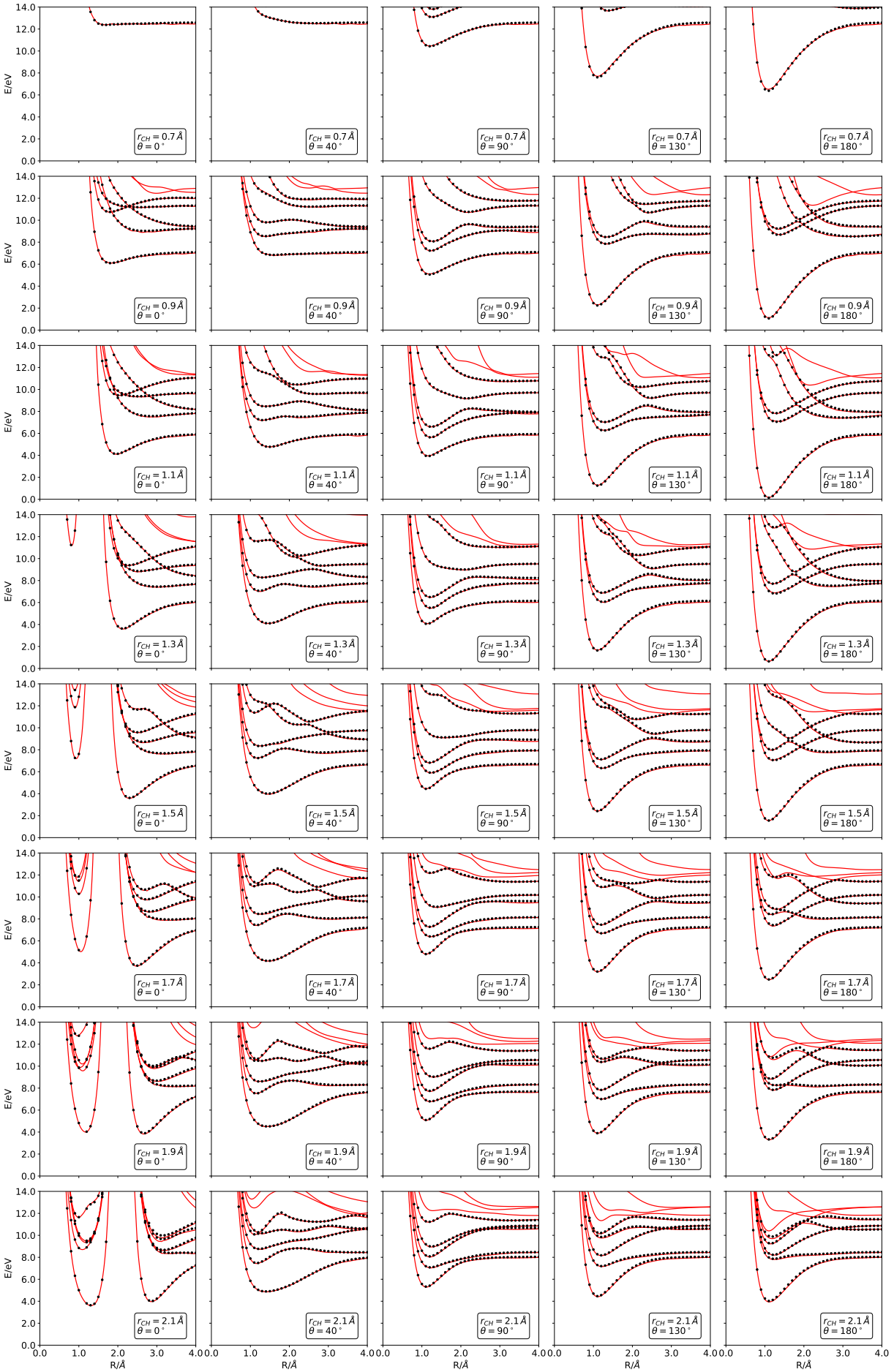

Figure 5: Adiabatic energies of the A'' states computed from the PEM (solid lines) compared with *ab initio* calculation of the five lowest adiabatic states. For each CH distance (r_{CH}) and H–C–H angle (θ) the second CH distance (R) is scanned.

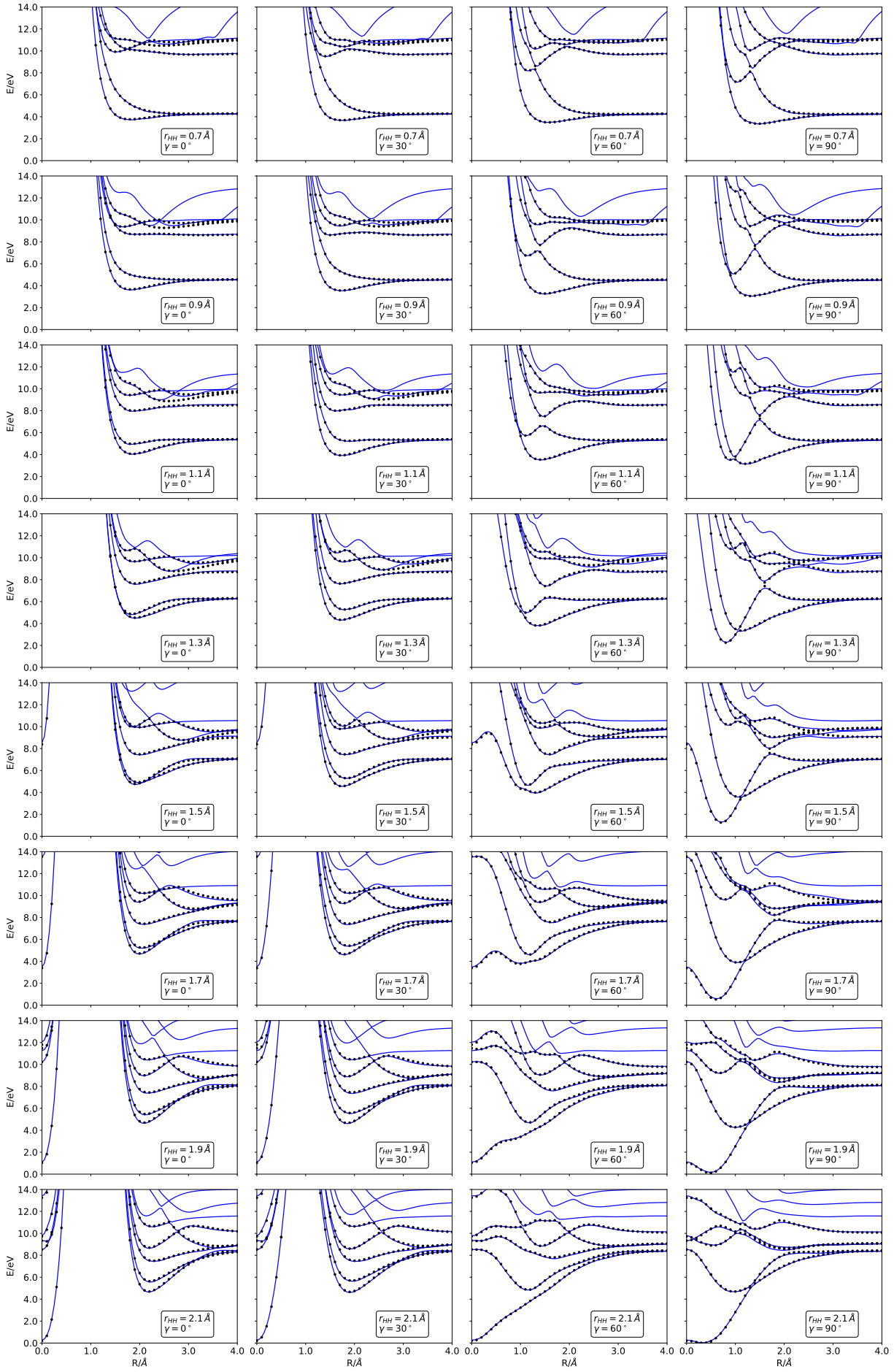

Figure 6: Adiabatic energies of the A' states computed from the PEM (solid lines) compared with *ab initio* calculation of the five lowest adiabatic states. For each HH distance (r_{HH}) and Jacobi angle for the $[C + H_2]^+$ system (γ) the R coordinate is scanned.

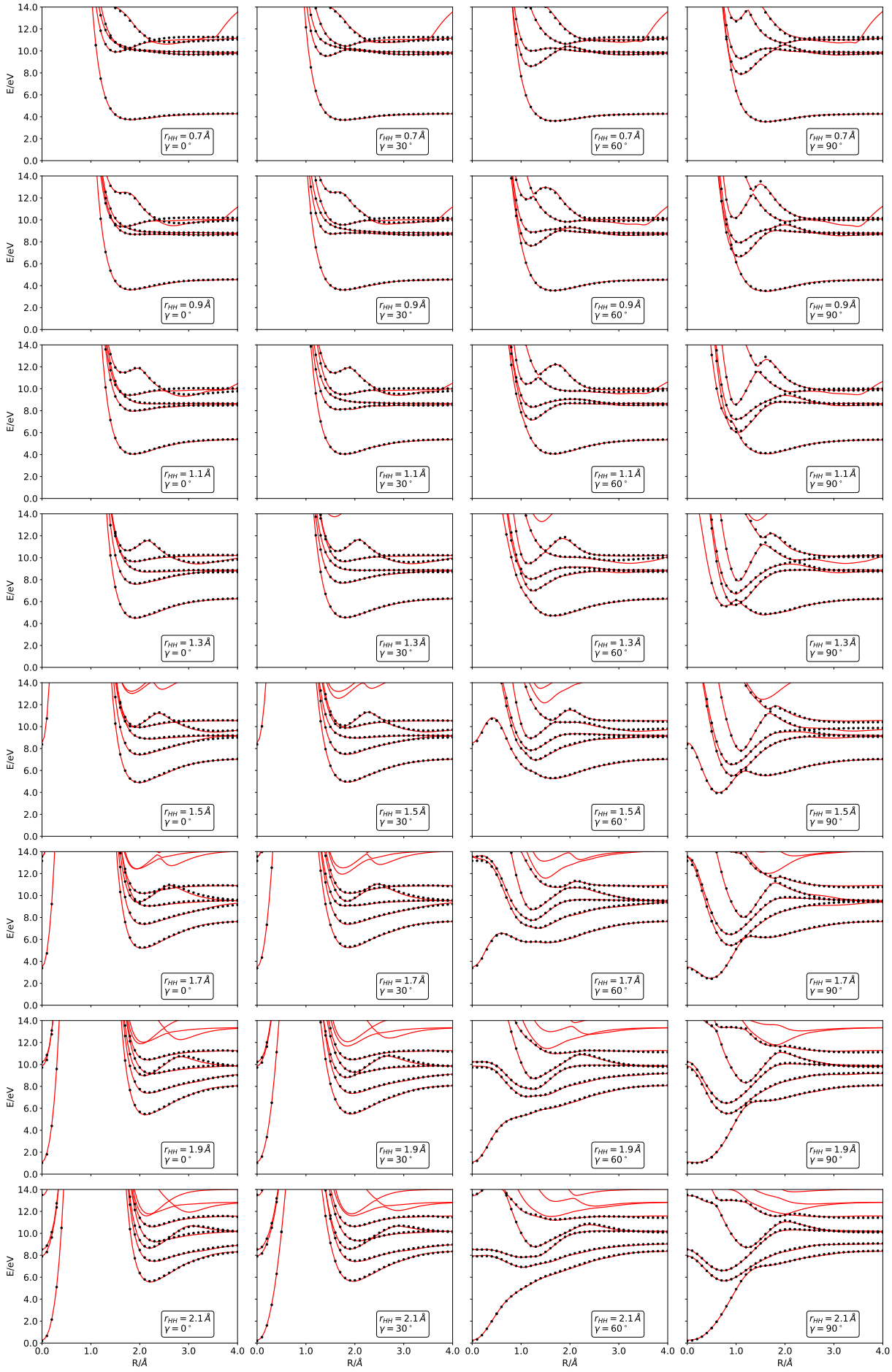

Figure 7: Adiabatic energies of the A'' states computed from the PEM (solid lines) compared with *ab initio* calculation of the five lowest adiabatic states. For each HH distance (r_{HH}) and Jacobi angle for the $[C + H_2]^+$ system (γ) the R coordinate is scanned.

accuracy of the initial bound states, new analytic full dimensional potential energy surfaces (PESs) have been developed to describe the $\widetilde{X}^2A'$ and the $\widetilde{A}^2A''$ lower adiabatic electronic states of CH_2^+. Two permutational invariant polynomial neural networks (PIP–NN)[5] take into account the exact permutation symmetry of the two hydrogen atoms for each electronic state. The training points are generated from grids of C-H distances ($d_{CH} = [0.5, 2.5]$Å) and H-C-H angles ($\theta = [1.00, 179.99]^\circ$). While many of these points are far from the CH_2^+ minima for both electronic states, they are necessary to avoid the appearance of spurious wells that would interfere with the bound state calculations. Still, in order to provide a highly accurate description of the wells we impose two energy constraints. First, only the geometries with an energy relative to the minimum in the $\widetilde{X}^2A'$ state of 3.5 eV are considered. Next, those with and energy larger than 2.5 eV will be weighted in the loss function with a factor of 10^{-7}. A weighted mean-squared error is employed in the training process:

$$L = \frac{1}{N}\sum_{i=1}^{N} w_i (E^*_{s,i} - E_{s,i})^2 \tag{7}$$

where $E^*_{s,i}$ is the *ab initio* energy for the ith geometry in the s electronic state, $E_{s,i}$ is the predicted energy and w_i is the weight assigned to that geometry.

Each neural network is a multilayer perceptron with a single hidden layer of dimension 40, which receives a set of 5 standardize PIP and outputs a single value, the energy. The PES RMSE errors for each state and computed with geometries with an energy up to 2.5 eV are presented in Table 1:

	$\widetilde{X}^2A'/\mathrm{cm}^{-1}$	$\widetilde{A}^2A''/\mathrm{cm}^{-1}$
ic-MRCI-F12	7.9	7.2
RCCSD(T)-F12a	6.4	7.1

Table 1: RMSE for the ic-MRCI-F12 and RCCSD(T)-F12a potential energy surfaces fitted in this work. The error is calculated for all the points with an energy lower or equal to 2.5 eV.

5 Initial Bound states

The total wave function, for a given total angular momentum J (and projection M) and a total parity under inversion of p is represented in CH+H Jacobi coordinates, also used for the photodissociation dynamics described below, in a body-fixed frame with the z-axis parallel to $\mathbf{R}$, as

$$\Psi^{JMp}(\mathbf{r},\mathbf{R}) = \sum_{\Omega\Lambda} \sqrt{\frac{2J+1}{8\pi^2}} D^{J*}_{M\Omega}(\alpha,\beta,\gamma)|\Lambda\rangle \frac{\Phi^J_\Omega(r,R,\gamma)}{rR}, \tag{8}$$

where Ω is the projection of $\mathbf{J}$ on the z-axis of the body fixed frame, and $|\Lambda\rangle$ represent the electronic adiabatic wave function. $\Lambda = 1$ is considered for the $\widetilde{X}^2A'$ and $\widetilde{A}^2A''$ electronic states.

The internal coordinates, r, R, γ, are described in grids, with $\cos\gamma = \mathbf{r}\cdot\mathbf{R}/rR$, with $\mathbf{r}$ being the internuclear vector joining H to C, while $\mathbf{R}$ goes from the HC center-of-mass to the second H atom. Equidistant points are used to describe the radial r_i coordinates, non-orthogonal Gauss-Legendre DVR[6,7] to describe γ. The bound state calculations are done using a non-orthogonal Lanczos method as implemented in the bndgrid program of the MADWAVE3 package[8].

The first 10 eigen-values for J=0 for the two electronic states are listed in Table 2, and compared with those obtained by Jensen *et al.*[9] Fig. 8 shows the representation of the potential energy surfaces as a function of the supplementary angle of γ, and the vibrational levels. The ground $\widetilde{X}^2A'$ electronic state has a small barrier to linearity, and at linearity becomes degenerate with the $\widetilde{A}^2A''$ electronic state forming a $^2\Pi_u$ state. The assignment in the two vibrational progressions is the same and the energy differences are better than 10 cm^{-1}, and the first 5 for each electronic states are shown in Fig. 9, showing the nodal structure allowing the assignment. The HC+H Jacobi coordinates used are non-symmetric under hydrogen permutation, but the CH center-of-mass is very close to C atom, and the probability distribution on r and R are very similar, allowing the clear identification of symmetric/antisymmetric states under hydrogen permutation.

$\widetilde{X}^2A'$			$\widetilde{A}^2A''$		
(v_1,v_2,v_3)	This work	Ref.[9]	(v_1,v_2,v_3)	This work	Ref[9]
(0,0,0)	0.00	0.0	(0,0,0)	2983.90	2980.1
(0,1,0)	994.83	995.6	(0,1,0)	5360.28	5350.0
(0,2,0)	2093.72	2093.1	(1,0,0)	5867.37	5866.3
(1,0,0)	2888.84	2899.5	(0,0,1)	6128.92	6130.2
(0,0,1)	3124.95	3131.4	(0,2,0)	7715.25	7699.1
(0,3,0)	3329.62	3327.1	(1,1,0)	8219.61	8212.3
(1,1,0)	3875.41	3386.9	(0,1,1)	8452.50	8443.9
(0,1,1)	4102.43	4109.5	(2,0,0)	8684.71	8689.2
(0,4,0)	4675.19	4672.2	(1,0,1)	8900.91	8906.2
(1,2,0)	4967.23	4974.7	(0,0,2)	9212.33	9219.9

Table 2: Vibrational energies (in cm^{-1}), with the zero of energy at the ground vibrational state of the ground electronic state $\widetilde{X}^2A'$, ZPE= 3637.328 cm^{-1}.

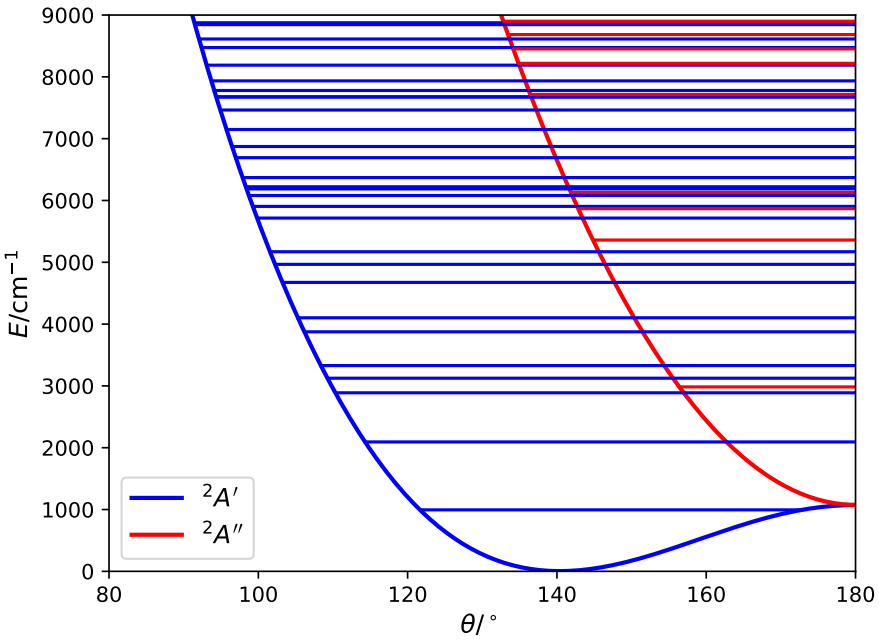

Figure 8: Graphical representation of vibrational levels computed, with $\theta = \pi - \gamma$.

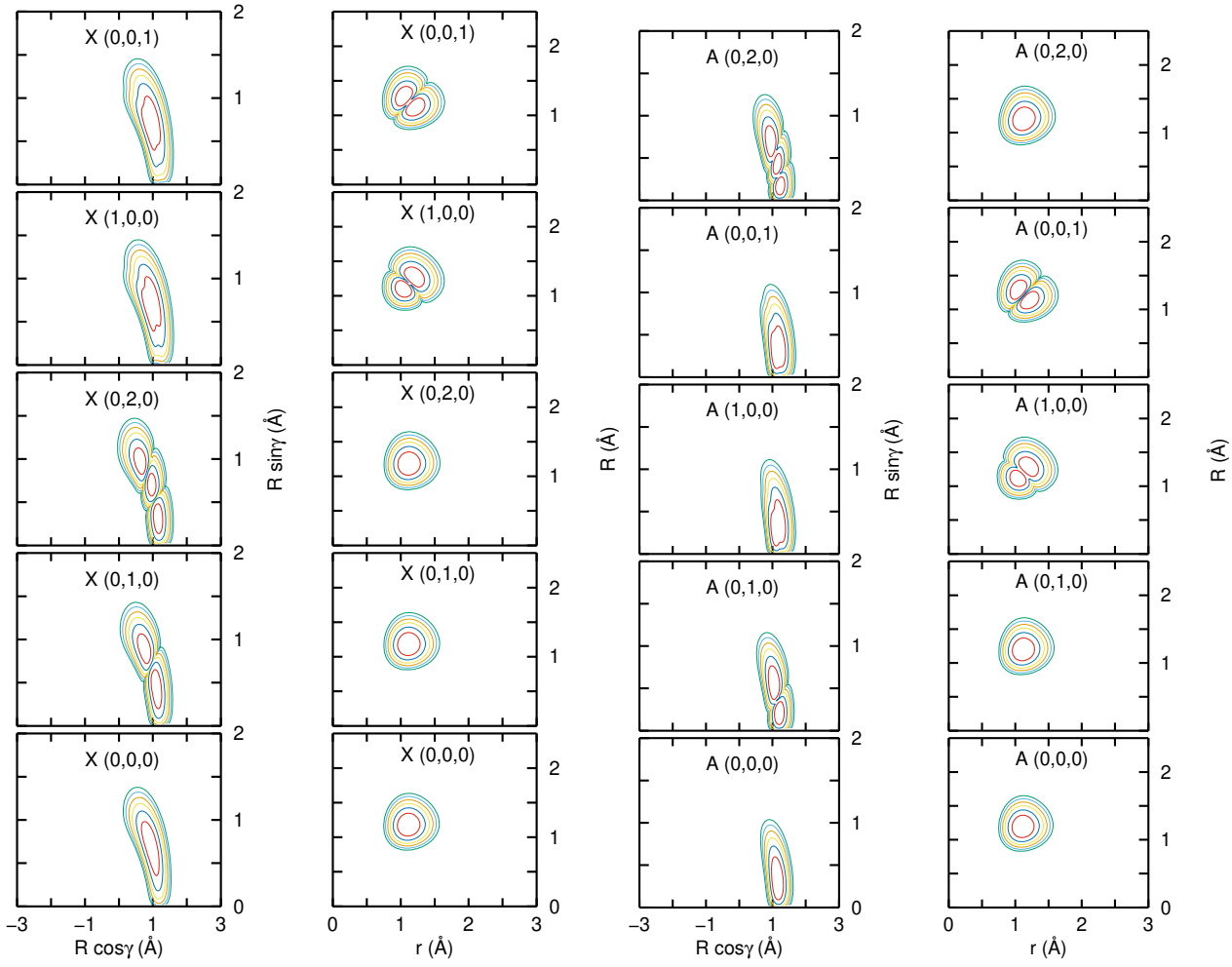

Figure 9: Contour plots of the density of the first 5 rovibronic states for $\widetilde{X}^2A'$ (left panels) and $\widetilde{A}^2A''$ (right panels) electronic states of CH_2^+ for J=0. Each contour is a tenth of the previous one.

6 Transition dipole matrix elements

The adiabatic transition dipole moments required to simulate the spectra from the lowest electronic states of CH_2^+ to the A' and A'' excited states, are calculated with the MOLPRO suite of programs,[10,11] using the MRCI-F12a method and the cc-pCVTZ-F12 basis set.

The values of the vertical electronic energy and the module of the transition dipole moments $\langle\phi_i|\hat{\mu}|\phi_j\rangle$ for the vertical transition from the ground electronic state, X^2A' to the four excited states of symmetry A' and A'' are given in Table 3. The present results of the vertical electronic differences are in good agreement with previous results,[12] with differences of about 0.1 eV. Also the calculated transition dipole moment for the process $\widetilde{A}^2B_1 \rightarrow \widetilde{X}^2A_1$ at the equilibrium geometry of the ground electronic state, is in very good agreement with the value 0.1039 a.u. reported previously.[12]

Note that the highest values correspond to the transition to the states $5^2A'$ (3^2A_1) and $4^2A''$ (2^2B_1). To understand this, we analyzed the electronic configuration of the states, shown in Table 3. In Fig. 10 we show the valence orbitals at the equilibrium geometry. Basically, orbital $2a'$ is a H_1-C-H_2 bonding orbital, $3a'$ orbital is a H_1-H_2 antibonding orbital, and $3a'$, $4a'$ and $1a''$ are like $2p$ orbitals of the carbon atom, in-molecular-plane the $3a'$ and $4a'$ and out-of-molecular-plane the $1a''$ molecular orbital.

State	Energy/eV	Electronic configuration	Dipole/a.u.
$\widetilde{X}^2A'$ ($\widetilde{X}^2A_1$)	0.	$\cdots(2a')^2(3a')^2(4a')^1$	0.273
$2^2A'$ (1^2B_2)	7.18	$\cdots(2a')^2(3a')^1(4a')^2$	0.059
$3^2A'$ (2^2B_2)	9.13	$\cdots(2a')^2(3a')^1(1a'')^2$	0.019
$4^2A'$ (2^2A_1)	10.37	$\cdots(2a')^2(3a')^2(5a')^1$	0.164
$5^2A'$ (3^2A_1)	12.83	$\cdots(2a')^1(3a')^2(4a')^2$	0.421
$\widetilde{A}^2A''$ ($\widetilde{A}^2B_1$)	0.82	$\cdots(2a')^2(3a')^2(1a'')^1$	0.103
$2^2A''$ (1^2A_2)	6.84	$\cdots(2a')^2(3a')^1(4a')^1(1a'')^1$	0.0
$3^2A''$ (2^2A_2)	7.51	$\cdots(2a')^2(3a')^1(4a')^1(1a'')^1$	0.0
$4^2A''$ (2^2B_1)	13.07	$\cdots(2a')^1(3a')^2(4a')^1(1a'')^1$	0.299
$5^2A''$ (3^2B_1)	15.56	$\cdots(2a')^2(3a')^2(2a'')^1$	0.141

Table 3: Vertical energies in eV, and the module of the transition dipole moment from the ground electronic state, $\widetilde{X}^2A'$, at the equilibrium geometry, to the excited electronic states, in atomic units. For the $\widetilde{X}^2A'$ the value is the permanent dipole moment.

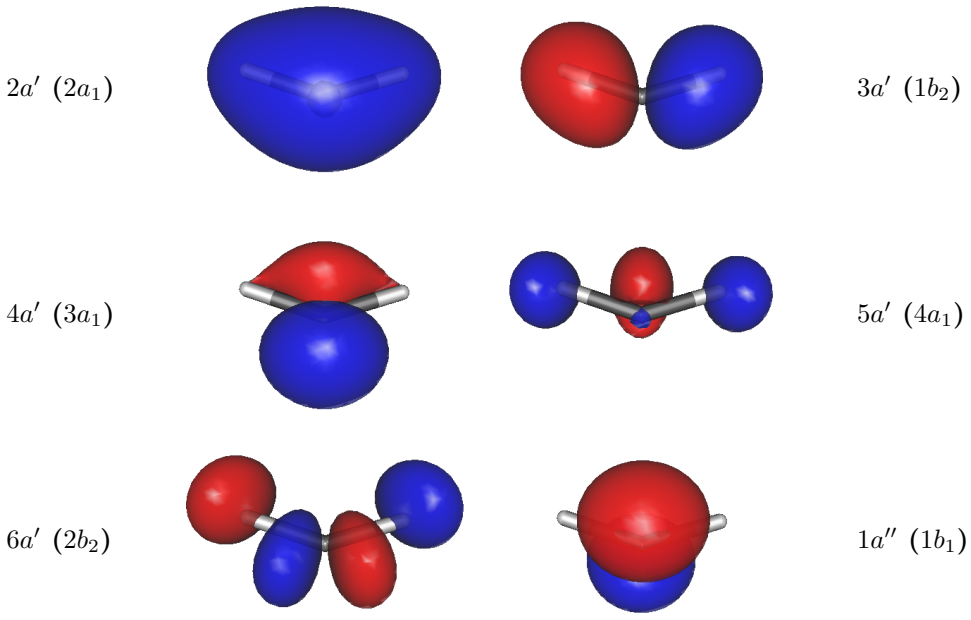

Figure 10: CASSCF valence orbitals at the equilibrium geometry of the ground electronic state $\widetilde{X}^2A'$ ($\widetilde{X}^2A_1$).

Because the contribution of carbon's $2p$ orbitals to the $3a'$, $4a'$, and $1a''$ molecular orbitals is high, the $\langle 2a'|\vec{r}|3a'\rangle$, $\langle 2a'|\vec{r}|4a'\rangle$, and $\langle 2a'|\vec{r}|1a''\rangle$ orbital integrals have great values, as a consequence of the angular node of the carbon's $2p$ orbitals. This explains why the highest transition dipole moment corresponds to a change in occupation from the $2a'$ orbital –with high contribution from the 2s orbital of C– to either $4a'$ or $1a''$ orbital.

In fact, because in the $\widetilde{X}^2A'$, $5^2A'$ and $4^2A''$states, the Mulliken Population analysis gives a small carbon charge, the transitions $\widetilde{X}^2A' \rightarrow 5^2A'$ and $\widetilde{X}^2A' \rightarrow 4^2A''$ are similar to the $(2s^1 2p^3)\,^3S \rightarrow (2s^2 2p^2)\,^3P$ transition in the neutral carbon atom, that appears at 13.11 eV.[13]

For the simulation of the spectra from the lowest excited electronic state $\widetilde{A}^2A''$, the transition dipole moments from the $\widetilde{A}^2A''$ to the other states are required. In Table 4 the values at the linear equilibrium geometry of the $\widetilde{A}^2\Pi_u$ state, are shown. In this case, the $4a'$ and $1a''$ orbitals have π character, being the other occupied orbitals of σ character. The ground electronic state electronic configuration of the degenerate $\widetilde{X}^2\Pi_u$ and $\widetilde{A}^2\Pi_u$ states is $(1\sigma_g)^2(2\sigma_g)^2(1\sigma_u)^2(1\pi_u)^1$, that in the C_s point group correspond to $(1a')^2(2a')^2(3a')^2(4a')^1$ for the $\widetilde{X}^2A'$ state and to $(1a')^2(2a')^2(3a')^2(1a'')^1$ for the $\widetilde{A}^2A''$ state, as shown in Table 4.

State	Energy/eV	Electronic configuration	Dipole/a.u.
$\widetilde{X}^2A'$ $(X^2\Pi_u)$	0.00	$\cdots(2a')^2(3a')^2(4a')^1$	0.0
$2^2A'$ $(1^2\Delta_u)$	7.97	$\cdots(2a')^2(3a')^1(4a')^2$ − $\cdots(2a')^2(3a')^1(1a'')^2$	0.0
$3^2A'$ $(1^2\Sigma_g^+)$	8.55	$\cdots(2a')^2(3a')^2(5a')^1$	0.020
$4^2A'$ $(1^2\Sigma_u^+)$	9.14	$\cdots(2a')^2(3a')^1(4a')^2$ + $\cdots(2a')^2(3a')^1(1a'')^2$	0.0
$5^2A'$ $(2^2\Sigma_u^+)$	12.56	$\cdots(2a')^2(3a')^2(6a')^1$	0.0
$6^2A'$ $(1^2\Delta_g)$	12.95	$\cdots(2a')^1(3a')^2(4a')^2$ + $\cdots(2a')^1(3a')^2(1a'')^2$	0.340
$\widetilde{A}^2A''$ $(A^2\Pi_u)$	0.00	$\cdots(2a')^2(3a')^2(1a'')^1$	0.0
$2^2A''$ $(1^2\Sigma_u^-)$	7.34	$\cdots(2a')^2(3a')^1(4a')^1(1a'')^1$	0.0
$3^2A''$ $(1^2\Delta_u)$	7.97	$\cdots(2a')^2(3a')^1(4a')^1(1a'')^1$	0.0
$4^2A''$ $(1^2\Delta_g)$	12.95	$\cdots(2a')^1(3a')^2(4a')^1(1a'')^1$	0.340
$5^2A''$ $(2^2\Pi_u)$	14.74	$\cdots(2a')^2(3a')^1(5a')^1(1a'')^1$	0.0

Table 4: Vertical energies in eV, and the module of the transition dipole moment from the first excited electronic state, $\widetilde{A}^2A''$, at the equilibrium geometry, to the other electronic states, in atomic units. For the $\widetilde{A}^2A''$ the value is the permanent dipole moment. In this case the zero of energy is set in the linear equilibrium geometry of the $A^2\Pi_u$ state.

The three Cartesian components of the adiabatic transition dipole moments between the lowest five A' and four A'' adiabatic states, have been fitted using one-dimensional splines for each CH + H Jacobi coordinate, where the body-fixed frame has the z-axis parallel to the distance of the Center-of-Mass of H_1C to the second hydrogen H_2, being the molecular plane the xz plane. To correct the sign of the phase of the adiabatic electronic wavefunctions, that can produce a change of sign in the transition dipole moments, the biorthogonal transformation –programmed in MOLPRO– is used to calculate the overlap between consecutive points along lines, as done previously for the CH_3^+ photodissociation study.[14] The representation of the dipole moment as a function of the R Jacobi coordinate is shown in Fig. 11. As expected, in the regions of avoided crossings between adiabatic electronic states there is an abrupt change in the dipole moment.

As discussed in the photodissociation section, the dynamics will be carried out in the diabatic representation, so in order to obtain the dipole moments in this representation, it is necessary to have the 2×16 dipole moment matrix, between the states $\widetilde{X}^2A'$ and $\widetilde{A}^2A''$ to all the A' and A'' states.

Note that while in the Frank-Condon region, the transitions from the ground electronic state to states $2^2A''$ (1^2A_2) and $3^2A''$ (2^2A_2) are forbidden by symmetry ($A_1 \not\rightarrow A_2$), there is a certain probability of transition since the dipole moment varies with the Jacobi coordinates, due to the loss of symmetry from C_{2v} to C_s. The same applies to the transition from the first excited state $\widetilde{A}^2A''$ to other electronic states. In this case, the allowed transitions from the equilibrium configuration of state $\widetilde{A}^2A''$ are those in which $\Delta\Lambda = 0, \pm 1$ and $u \longleftrightarrow g$, as shown in Table 4. Since the maximum of the density in the $\widetilde{A}^2A''$ state is at $\gamma = 15°$, in the variation of the r and R distances, the transition dipole moments have been calculated at this angle.

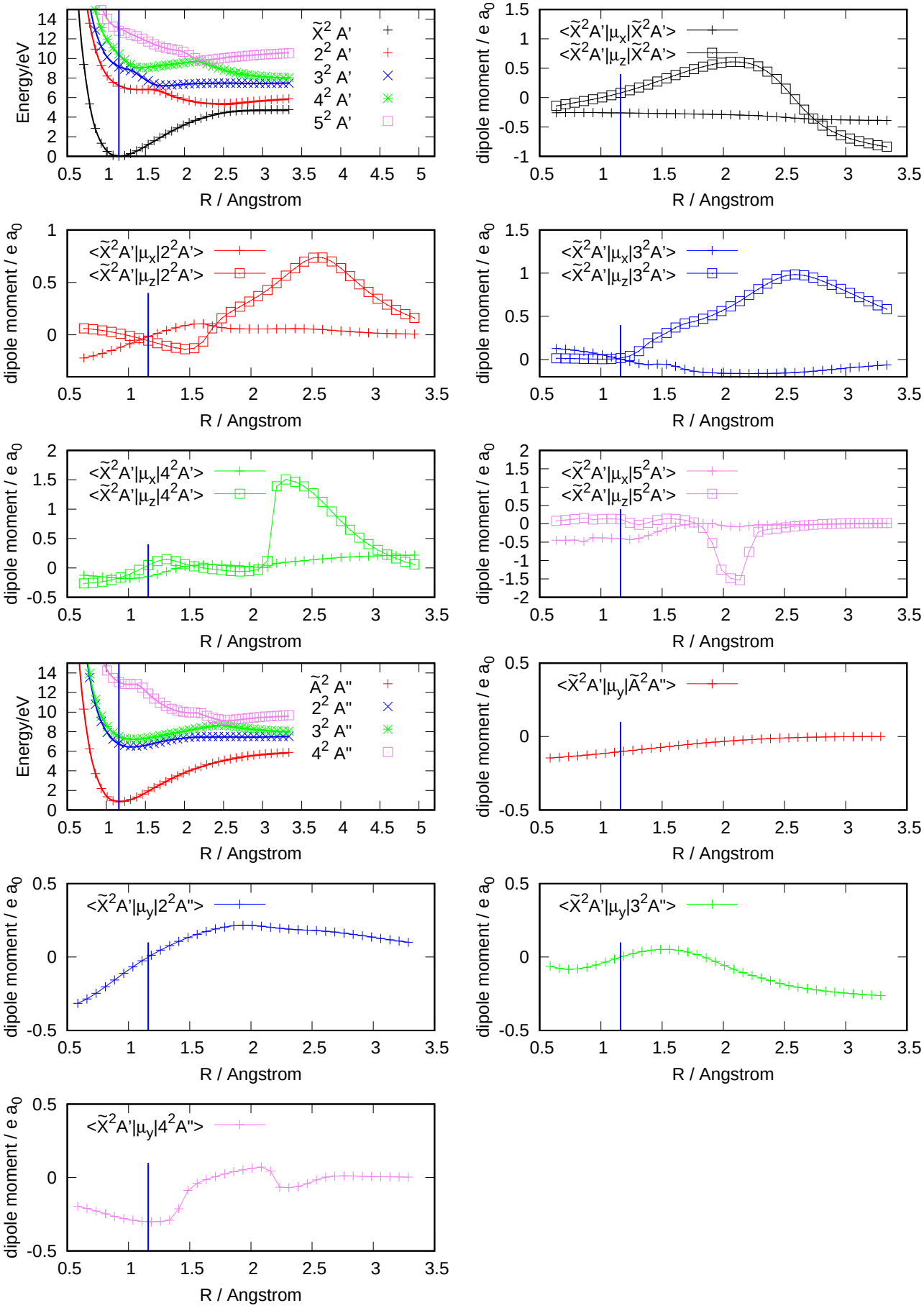

Figure 11: Dipole moments as a function of the Jacobi R distance, in atomic units. The vertical blue line indicates the Franck-Condon region.

7 Photodissociation

The parameters used in the wave packet dynamics are listed in Table 5. Calculations for the $J_i = 0 \longrightarrow J = 1^-$ rotational transitions are done for the 8×8 diabatic electronic states ans also on each adiabatic electronic state.

$r_1^{min}, r_1^{max}, n_1$	0.1, 10 , 512
$r_2^{min}, r_2^{max}, n_2$	0.1, 10 , 512
n_γ	120
$\alpha_1^{abs}, r_1^{abs}, n_1^{abs}$	0.005,7.5,4
$\alpha_2^{abs}, r_2^{abs}, n_2^{abs}$	0.005,7.5,4
r_1^{flux}	6.
V_{cut}	15

Table 5: Parameters used in the MADWAVE3 for the wave packet photodissociation dynamics. An explanation of the parameters are found in[8]. Distances are in Å, energy in eV.

The assignment of the bands is done by comparing the spectra to those obtained in the adiabatic representation, in Fig. 12, for the transition from the $\widetilde{X}(0,0,0)$ and $\widetilde{A}(0,0,0)$ bound states towards each excited adiabatic states individually. Clearly, the most intense peak are those arriving to $5A'$ and $4A''$ electronic state, because these excited states have considerably larger transition dipole moments with $\widetilde{X}^2A'$ and $\widetilde{A}^2A''$ states than the other electronic states at lower energies.

The threshold in the adiabatic representation start at higher energies than those associated to the coupled diabatic states. In the adiabatic representation there is no coupling to the lower electronic states, either $1^2A'$ or $1^2A''$, and therefore the flux is collected only from their respective thresholds. This is clearly justifies the need of including non-adiabatic transitions.

The transitions towards the 8 A'' states show a drop around 10 eV, which is clearly attributed to the energy separation among the A'' states, less dense packed than the A' states.

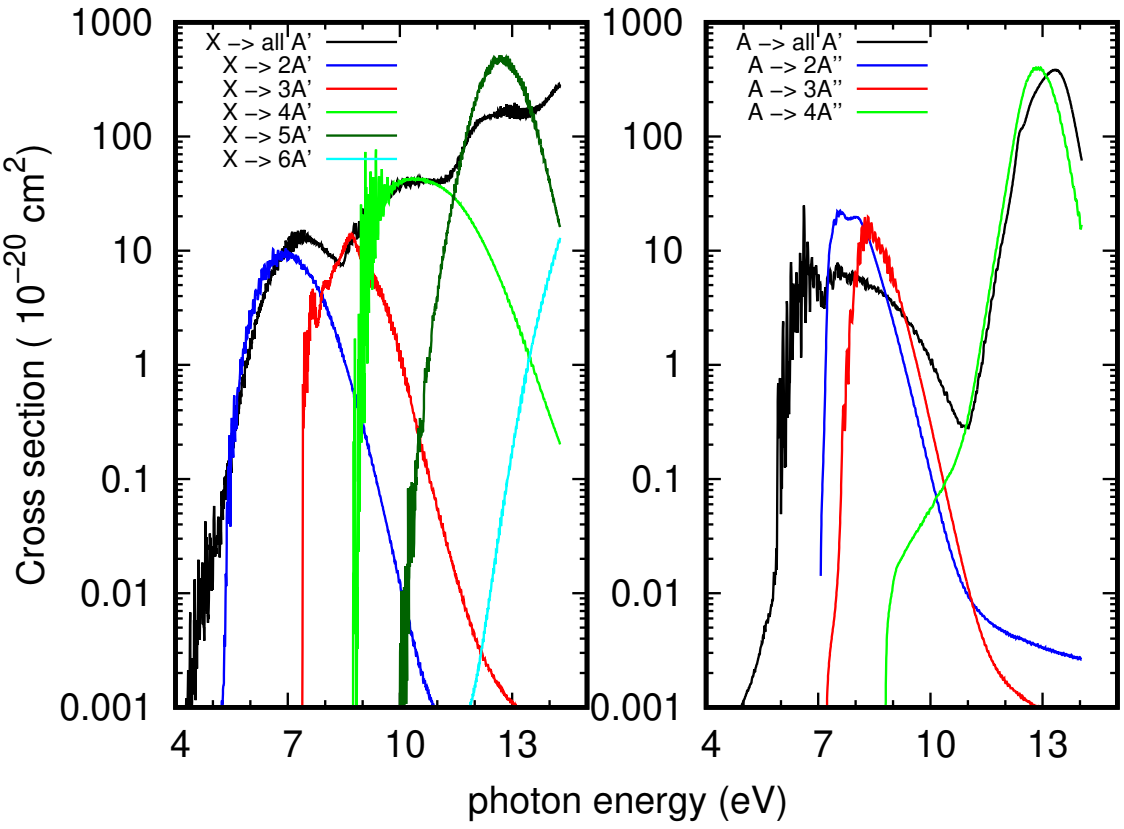

Figure 12: Photodissociation cross sections using adiabatic to adiabatic transitions, from the $\widetilde{X}^2A'(0,0,0)$ to the 2,3 and 4 A' states (left panel) and from the $\widetilde{A}^2A''$(0,0,0) to the 2,3 and 4 A" electronic (right panel). In each case the total spectra to the 8 diabatic A' (left) and A" (right) is shown for comparison

The fluxes obtained obtained from the ground vibrational level of the $\widetilde{A}^2A''$ are shown in Fig. 13. The fluxes from $\widetilde{A}^2A''$ show many similarities with those from $\widetilde{X}^2A'$. The main difference is in the $\widetilde{A}^2A'' \longrightarrow A''$

transitions, which are less intense around 13 eV. This is due to the lower $\widetilde{X}^2A' \longrightarrow 4A''$ transition dipole moment, which is significantly reduced in the Frank-Condon region because of an avoided crossing with the $5A''$ adiabatic state.

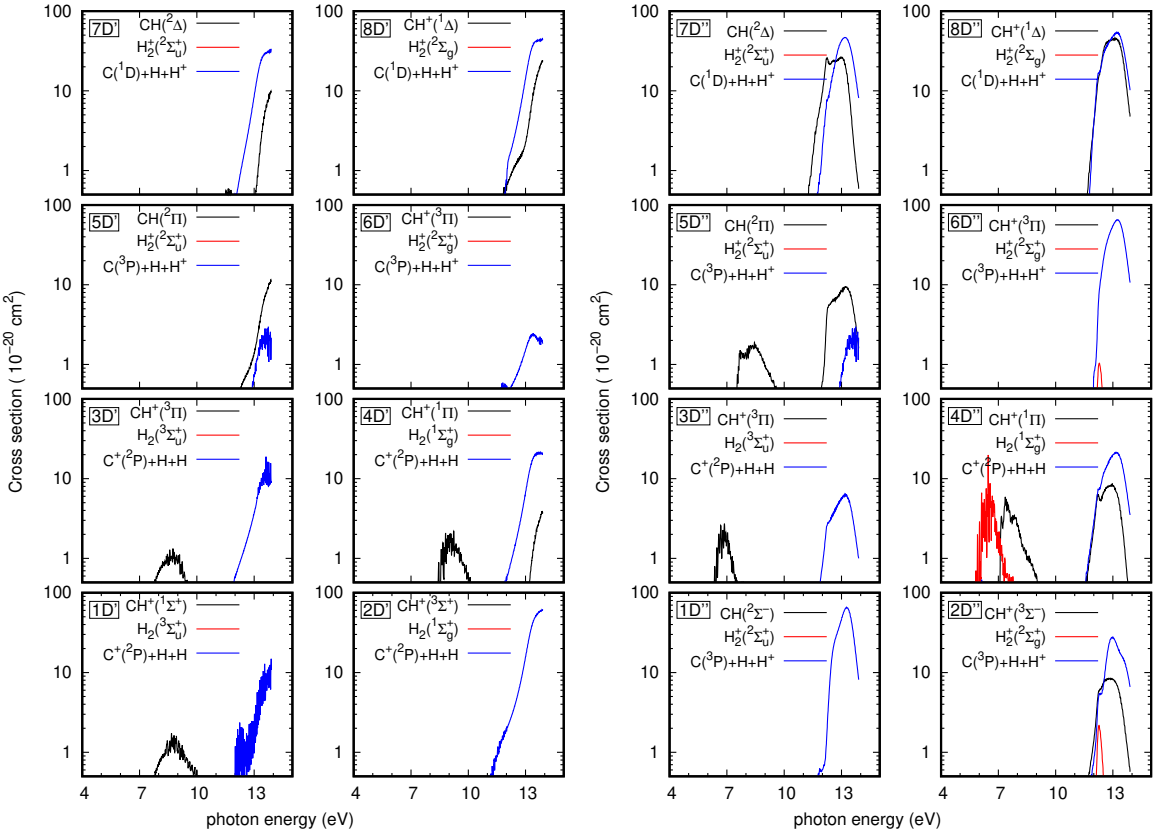

Figure 13: Photodissociation cross sections for the $\widetilde{A}^2A''(0,0,0) \longrightarrow$ all D' states and all D'' states, as indicated in each panel, separating individual fluxes for the different fragments of each rearrangement channel in each electronic state, as discussed in the text.

8 CH^+

The electronic absorption spectra of the CH^+ molecule has been obtained. For that, several singlet potential energy curves and transition dipole moments were calculated *ab initio* using an aug-cc-pVTZ atomic basis set, and a CASSCF(4,5)/MRCI method with the MOLPRO package of program.[10] As done previously for other systems,[14] the sign of the phase of the adiabatic of the transition dipole moment eigenvectors was also corrected. All calculations were done in the C_{2v} point group of symmetry.

The upper panel of Fig.14 shows the potential energy curves for the CH^+ molecule. Solid lines correspond to our calculations and dashed lines to the potential energy curves calculated by Saxon et al.[15] Transition dipole moments from the ground electronic state, $X^1\Sigma^+$, to the dipole-allowed excited states are shown in the bottom panel of the same figure.

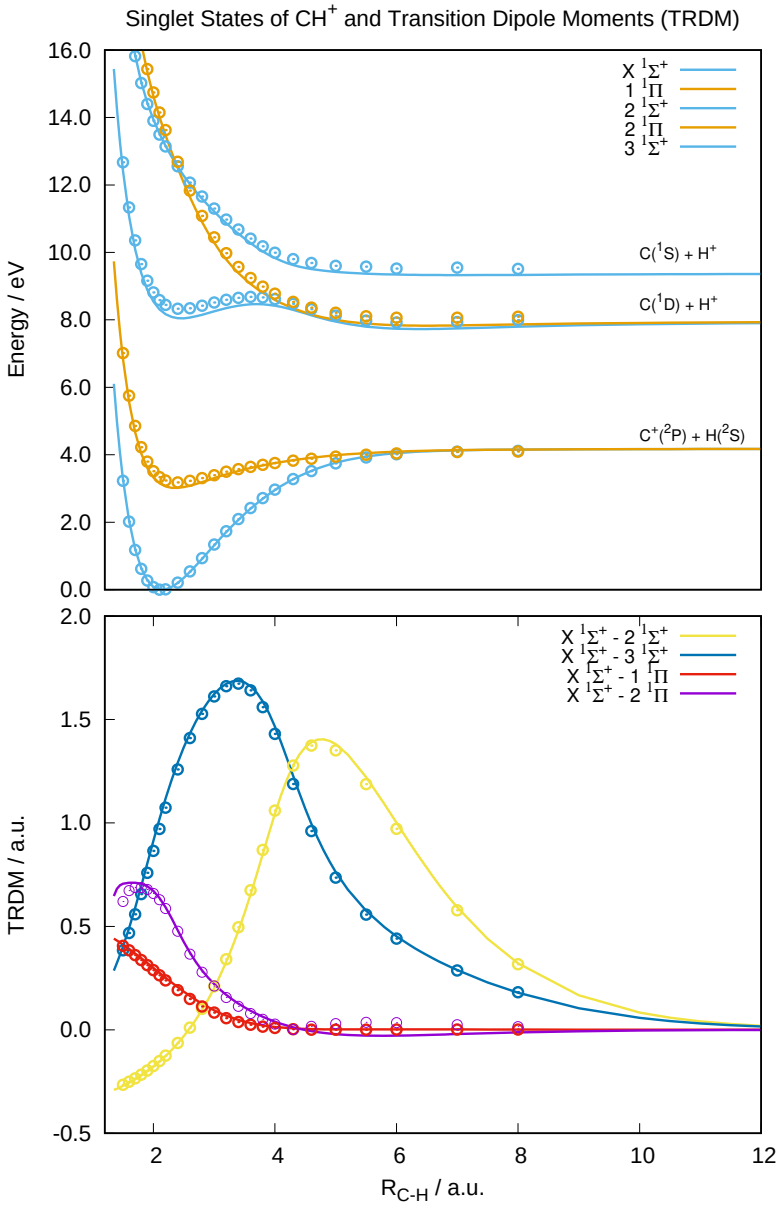

Figure 14: Upper panel: potential energy curves for the CH^+ radical. Energies are given in eV and bond distances in a.u.; Lower panel: Transition dipole moments from the $X^1\Sigma^+$ ground electronic state to the $2^1\Sigma^+$, $3^1\Sigma^+$, $1^1\Pi$ and $2^1\Pi$ excited states. Dashed lines correspond to the results by Kirby et al.[15]

The absorption cross section was calculated by using the MADWAVE3 program,[8] a code for quantum dynamical calculations using wavepackets. Fig. 15 shows the absorption cross sections (in a logarithmic scale) as a function of the photon energy for the transition from the ground electronic state of CH^+ to each of the adiabatic excited ones.

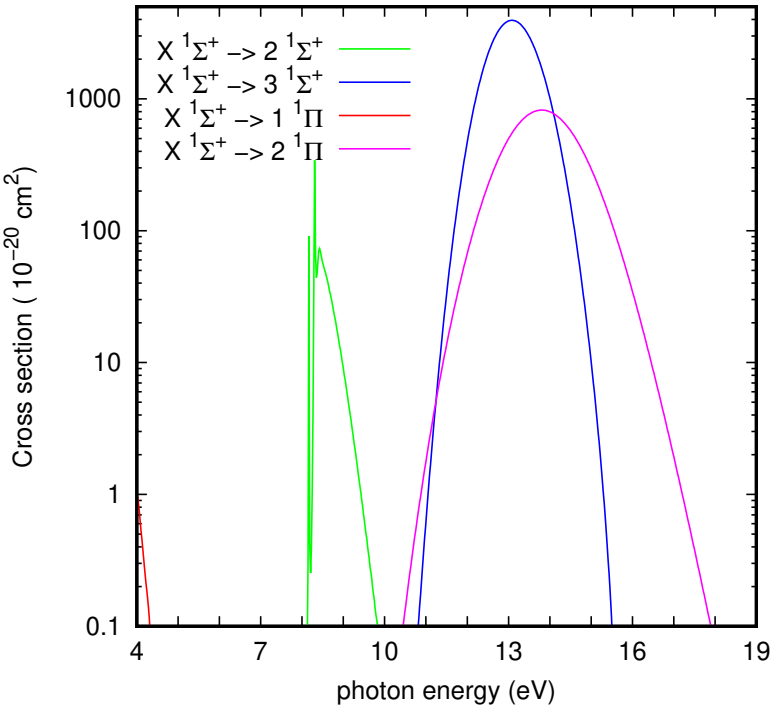

Figure 15: Calculated photoabsorption spectrum (in logarithmic scale) of the CH^+ radical.

References

[1] A. Aguado and M. Paniagua, *J. Chem. Phys.*, 1992, **96**, 1265.

[2] L. Velilla, B. Lepetit, A. Aguado, J. A. Beswick and M. Paniagua, *The Journal of Chemical Physics*, 2008, **129**, 084307.

[3] I. Loshchilov and F. Hutter, *Decoupled Weight Decay Regularization*, 2019, `https://arxiv.org/abs/1711.05101`.

[4] A. Paszke, S. Gross, F. Massa, A. Lerer, J. Bradbury, G. Chanan, T. Killeen, Z. Lin, N. Gimelshein, L. Antiga, A. Desmaison, A. Kopf, E. Yang, Z. DeVito, M. Raison, A. Tejani, S. Chilamkurthy, B. Steiner, L. Fang, J. Bai and S. Chintala, Advances in Neural Information Processing Systems 32, 2019, pp. 8024–8035.

[5] B. Jiang and H. Guo, *J. Chem. Phys.*, 2013, **139**, 054112.

[6] G. C. Corey and D. Lemoine, *J. Chem. Phys.*, 1992, **97**, 4115.

[7] G. C. Corey, J. W. Tromp and D. Lemoine, *Numerical grid methods and their application to Schrödinger equation*, Kluwer Academic Publishers, 1993, p. 1.

[8] O. Roncero and P. del Mazo-Sevillano, *Comp. Phys. Comm.*, 2025, 109471.

[9] P. Jensen, M. Brumm, W. P. Kraemer and P. R. Bunker, *J. Mol. Spectros.*, 1995, **172**, 194.

[10] MOLPRO is a package of ab initio programs designed by H. -J. Werner and P. J. Knowles and with contributions from , *J. Almlöf and R. D. Amos and A. Berning and M. J. O. Deegan and F. Eckert and S. T. Elbert and C. Hampel and R. Lindh and W. Meyer and A. Nicklass and K. Peterson and R. Pitzer and A. J. Stone and P. R. Taylor and M. E. Mura and P. Pulay and M. Schütz and H. Stoll and T. Thorsteinsson and D. L. Cooper*, version 2012.

[11] H.-J. Werner, P. J. Knowles, G. Knizia, F. R. Manby and M. Schütz, *WIREs Comput Mol Sci*, 2012, **2**, 242–253.

[12] G. Theodorakopoulos and I. D. Petsalakis, *J. Mol. Structure (Theochem)*, 1991, **230**, 205.

[13] I. Labazan, E. Reinhold, W. Ubachs and V. V. Flambaum, *Physical Review A*, 2005, **71**, 040501(R).

[14] P. del Mazo-Sevillano, A. Aguado, J. R. Goicoechea and O. Roncero, *J. Chem. Phys.*, 2024, **160**, 184307.

[15] R. P. Saxon, K. Kirby and B. Liu, *J. Chem. Phys.*, 1980, **73**, 1873.